

Magphan Phantoms for MR for radiation therapy and quantitative imaging applications.



Smári



Sub-voxel geometric distortion measurements
and critical image quality metrics engineered for
ease of use in the clinical workflow.

The Phantom Laboratory manufactures high-precision phantoms
coupled with Smári image analysis service and innovative custom
solutions for the medical imaging and radiation therapy fields.

[Click to see our latest phantoms and schedule a demo
of our Smári image analysis service.](#)

MS. ISABELL K. BONES (Orcid ID : 0000-0002-7916-5013)

MISS SUZANNE L FRANKLIN (Orcid ID : 0000-0001-6886-5578)

DR. ANITA A HARTEVELD (Orcid ID : 0000-0002-3379-0710)

PROF. MATTHIAS JP VAN OSCH (Orcid ID : 0000-0001-7034-8959)

MS. SOPHIE SCHMID (Orcid ID : 0000-0003-0750-7798)

Article type : Research Article (MP)

Improving the characterization of meningioma microstructure in proton therapy from conventional apparent diffusion coefficient measurements using Monte Carlo simulations of diffusion MRI

Giulia Buizza^{1,a}, Chiara Paganelli¹, Francesco Ballati², Simone Sacco², Lorenzo Preda^{3,b}, Alberto Iannalfi⁴, Daniel C. Alexander⁵, Guido Baroni^{1,6}, Marco Palombo⁵

¹ Department of Electronics, Information and Bioengineering (DEIB), Politecnico di Milano, 20133 Milan, Italy

² Diagnostic Radiology Residency School, University of Pavia, 27100 Pavia, Italy

³ Department of Clinical, Surgical, Diagnostic and Pediatric Sciences, University of Pavia, 27100 Pavia, Italy

⁴ Clinical Department, National Center of Oncological Hadrontherapy (CNAO), 27100 Pavia, Italy

⁵ Centre for Medical Image Computing (CMIC), Department of Computer Science, University College London (UCL), WC1V6LJ London, UK

⁶ Bioengineering Unit, National Center of Oncological Hadrontherapy (CNAO), 27100 Pavia, Italy

This article has been accepted for publication and undergone full peer review but has not been through the copyediting, typesetting, pagination and proofreading process, which may lead to differences between this version and the [Version of Record](#). Please cite this article as [doi: 10.1002/MP.14689](https://doi.org/10.1002/MP.14689)

This article is protected by copyright. All rights reserved

^a Corresponding author: Giulia Buizza – address: piazza Leonardo da Vinci 32, 20133 Milano, Italy – email: giulia.buizza@polimi.it – phone: +390223999022

^b Additional current affiliation: Department of Radiology, Fondazione IRCCS Policlinico San Matteo, 27100 Pavia, Italy

Running title: Microstructure characterization from ADC

ABSTRACT

Purpose. Proton therapy could benefit from non-invasively gaining tumour microstructure information, at both planning and monitoring stages. The anatomical location of brain tumours, such as meningiomas, often hinders the recovery of such information from histopathology, and conventional non-invasive imaging biomarkers, like the apparent diffusion coefficient (ADC) from diffusion-weighted MRI (DW-MRI), are non-specific. The aim of this study was to retrieve discriminative microstructural markers from conventional ADC for meningiomas treated with proton therapy. These markers were employed for tumour grading and tumour response assessment.

Methods. DW-MRI from patients affected by meningioma and enrolled in proton therapy were collected before (n=35) and three months after (n=25) treatment. For the latter group, the risk of an adverse outcome was inferred by their clinical history. Using Monte Carlo methods, DW-MRI signals were simulated from packings of synthetic cells built with well-defined geometrical and diffusion properties. Patients' ADC was modelled as a weighted sum of selected simulated signals. The weights that best described a patient's ADC were determined through an optimization procedure and used to estimate a set of markers of tumour microstructure: diffusion coefficient (D), volume fraction (vf) and radius (R). Apparent cellularity (ρ_{app}) was estimated from vf and R for an easier clinical interpretability. Differences between meningothelial and atypical subtypes, and low- and high-grade meningiomas were assessed with non-parametric statistical tests, whereas sensitivity and specificity with ROC analyses. Similar analyses were performed for patients showing low- or high-risk of an adverse outcome to preliminary evaluate response to treatment.

Results. Significant ($p < 0.05$) differences in median ADC, D, vf, R and ρ_{app} values were found when comparing meningiomas' subtypes and grades. ROC analyses showed that estimated microstructural parameters reached higher specificity than ADC for subtyping (0.93 for D and vf vs. 0.80 for ADC) and

grading (0.75 for R vs. 0.67 for ADC). High- and low-risk patients showed significant differences in ADC and microstructural parameters. The skewness of ρ_{app} was the parameter with highest AUC (0.90) and sensitivity (0.75).

Conclusions. Matching measured with simulated ADC yielded a set of potential imaging markers for meningiomas grading and response monitoring in proton therapy, showing higher specificity than conventional ADC. These markers can provide discriminative information about spatial patterns of tumour microstructure implying important advantages for patient-specific proton therapy workflows.

Keywords: Diffusion MRI, Particle therapy, Quantitative imaging, Microstructure, Meningioma

1 INTRODUCTION

During the last decade, proton therapy has seen an exponential growth with about 90 operational centres worldwide and over 40 under construction, to date (<https://www.ptcog.ch/>). Such development is due to protons providing higher biological effectiveness and geometrical selectivity with respect to conventional X-ray radiotherapy^[1], leading to increase the dose to tumours while sparing surrounding organs at risk. In this context, routinely acquired imaging plays a relevant role in guiding treatment planning and delivery^[2], and it is expected to non-invasively provide quantitative details at multiple spatial scales, which may be particularly relevant for optimized treatments of brain tumours. However, to date, the potentials of quantitative imaging in radiotherapy, and especially proton therapy, is not fully exploited^[3].

Meningioma is one of the most common intracranial tumours and can be classified in three grades of malignancy and 15 subtypes, according to the WHO, by evaluating mitotic and structural features (e.g. nuclear-to-cytoplasm ratio) from histopathological examinations^[4]. Surgical resection is the preferred treatment for low-grade meningiomas, with prognosis partially correlating to the extent of the resection^[5]. For high-grade or recurrent low-grade meningiomas, conventional radiotherapy^[6] and proton therapy^[7] are often administered in combination with surgery or alone, in case of inoperable tumours, with proton therapy rising worldwide^[8,9]. When the histopathological characterization is not available or limited, information for clinical decisions, such as the type of treatment or of radiation to deliver and the protocol to follow, must be heavily based on radiological imaging and clinical factors.

Despite the standardization efforts in both radiological and histopathological imaging, prognostic quantitative biomarkers are lacking^[10] and integration of multi-scale information relating tumour appearance to its microstructure needed^[11]. Quantitative imaging, such as diffusion-weighted MRI (DW-MRI), could reduce grading uncertainties^[12] by complementing molecular information from histological exams and clinical evaluations based on anatomical MRI^[13,14]. Several studies investigated the potential of DW-MRI to stratify patients according to tumour grade^[15] or response to radiotherapy^[16], exploiting advanced (e.g. diffusion tractography, DTI, or diffusion kurtosis, DKI^[17]) or more conventional^[12] MR sequences and by estimating structural features (e.g. cell size, shape or density) to describe the whole tumour and/or its microenvironments and heterogeneities^[18–20].

DW-MRI lends itself to characterizing tissue structure at the cellular level (namely microstructure), by measuring the mobility of endogenous water molecules. The spatial arrangement of cellular components and membranes impacts the displacement of water molecules, enabling DW-MRI to be sensitive to important microstructural features, such as cell density, size, shape and others^[21,22]. This microstructural

information, also represented as a set of biomarkers^[23], is inferred from DW-MRI signals through models of water diffusion^[24]: from the gaussian model, which consists of a mono-exponential decay of the DW-MRI signal and leads to the Apparent Diffusion Coefficient (ADC), the complexity is increased in multi-compartment and non-gaussian models^[25]. Such models can more specifically distinguish different diffusion and microstructural configurations, which the ADC alone cannot do. Among these models, diffusion kurtosis or bi-exponential models statistically represent the DW-MRI signal and provide parameters not specific to microstructure^[24]. Others, such as VERDICT^[26], Intra-Voxel Incoherent Motion (IVIM)^[27], and more^[28], interpret the underlying tissue biology to provide information about compartment diffusivities, vascularity, permeability or cellular density and dimensions. The richer description, while retaining robustness and reliability of the estimates, comes at the cost of complex imaging sequences and extended acquisition times. These specifications are often not compatible with clinical radiotherapy workflows that typically implement standard DW-MRI protocols (i.e. mono-exponential) in which, anyway, coarse microstructural information is encoded.

Estimating tissue microstructure features from routinely acquired DW-MRI data of patients enrolled for proton therapy would thus enable the inclusion of patient-specific microstructural information at the planning stage, and the longitudinal analysis of microstructural markers would certainly provide further insights into tumour response to treatment. This could substantially improve advanced radiotherapy treatments, such as proton therapy, which strongly benefit from personalized, optimized and accurate procedures^[29–31], leading to dose escalation strategies and advances in knowledge in how radiation induces changes in tissue.

The aim of this study is to recover markers of tumour microstructure from routinely acquired ADC of patients affected by meningioma tumours enrolled in proton therapy. Towards this goal, we obtained markers more specific to differences in tumour microstructure than ADC by searching for the set of microstructural parameters that best describes patients' ADC, from a dictionary of Monte Carlo simulations of DW-MRI signals obtained from pre-computed synthetic cellular packings. These analyses are put forward to derive meningioma microstructure characteristics before treatment, as well as to preliminary investigate early microstructural changes due to proton therapy.

2 MATERIALS AND METHODS

2.1 PATIENT DATA

Thirty-five patients affected by meningioma and enrolled for proton therapy at the National Center of Oncological Hadrontherapy (CNAO, Pavia, Italy) were retrospectively selected. The study was approved by an institutional review board and informed consent collected. For all of them information about tumour grade and sub-type was verified by a biopsy, whereas for 25 of them the risk (low vs. high) of adverse outcome three months after therapy was inferred from their one-year follow-up history. Clinical data is reported in Table 1. DW-MRI (b -values=0,200,400,1000 s/mm²; resolution 0.975x0.975x4mm) averaged along three orthogonal directions was acquired on a 3T scanner (Magnetom Verio, Siemens, Erlangen, Germany) before (n =35) and three months after (n =25) treatment (Figure S1-S2). After applying 2D rigid motion correction across b -values (Plastimatch v1.6^[32]), mono-exponential ADC maps were computed using different sets of b -values (b =200,1000; b =400,1000; b =200,400,1000 s/mm²). Gross tumour volume (GTV) contours were manually delineated on post-Gadolinium T1-weighted MRI, rigidly registered to DW-MRI, and manually adjusted according to b_0 and ADC images, taking care of retaining only the core tumour volume and excluding regions showing oedema.

2.2 SIMULATED DATA

Synthetic substrates comprised of packed cells mimicking tumour tissue microstructure of 100x100x100 μm^3 volume (Figure S3-S4) were generated by randomly packing ellipsoids with well-controlled density and plausible geometrical properties (Table 2) inferred from the available literature^[33,34]. The molecular dynamics algorithm proposed by Donev et al.^[35] was used to generate the best random configuration of ellipsoids satisfying a chosen set of values for volume fraction (vf), radius (R) and eccentricity. The resulting cellular packings were converted into three-dimensional surface meshes and periodically replicated in all directions in space (Blender v2.79^[36]) to avoid artefacts due to ceiling or the finite size of the simulated volume (100³ μm^3).

From these substrates, water molecules trajectories were simulated with a Monte Carlo approach using the Camino toolbox^[37] and assigning various combinations of diffusion (D) and cell membrane permeability values (Table 2, Figure 1A). Finally, a total of 3928 DW-MRI signals were computed by phase accumulation^[38] according to a DW-MRI sequence matching the acquired data (Figure 1B). Each simulated signal was thus associated to specific geometric (vf , R) and diffusion (D) properties.

2.3 FROM ADC TO MICROSTRUCTURAL MARKERS

To account for tissue heterogeneity within each MRI voxel and the ambiguous relationship between the measured ADC and the underpinning tissue microstructure (i.e., many different microstructure scenarios lead to the same ADC value), patient data was modelled as the weighted sum of simulated signals (Figure 1C), where each weight quantified the relative contribution of the corresponding simulated cell packings.

To retain a sparse and tractable representation of microstructures providing similar ADCs, simulated data was partitioned by means of a k-means algorithm (Figure 1C, i). Each partition was described by a centroid in the ADC space (Figure 1C, ii) and by distributions of microstructural parameters (Figure 1C, iii), estimated from all the partition members. The number of partitions (K) was chosen through an iterative process as the one that maximized the pairwise separation of the selected microstructural features distributions (D, vf, R) across clusters (Mann-Whitney U-test, $\alpha=0.05$). We tested initial K values from 2 to 10 and found that K=4 was the simplest configuration maximizing the pairwise separation.

Then, the set of weights that best combined the K clusters of simulated signals to match patients' ADC was found by minimizing, for each patient separately, a LASSO-regularized cost function (Figure 1C, iv):

$$\underset{w^{pt}}{\operatorname{argmin}} \left\{ \sum_{j=0}^2 (ADC_j(w^{pt}) - ADC_j^{pt})^2 + \lambda \|w^{pt}\|_1 \right\}$$

where ADC_j^{pt} represents the j^{th} ADC (e.g. ADC (200,1000)) value of the pt^{th} patient, λ the strength of the LASSO constraint and $\|\cdot\|_1$ the L1 norm. ADC_j^{sim} refers to the j^{th} ADC value coming from the K partitions of the simulated data, which depends on the unknown weight vector w^{pt} and is defined as:

$$ADC_j(w^{pt}) = \frac{1}{\Delta b_j} \cdot \log \left(\sum_k w_k \frac{S_{j,k}^{\text{high}}}{S_{j,k}^{\text{low}}} \right)$$

where $k=0, \dots, K-1$ refers to the partition number, Δb_j to the difference between the highest and lowest b-value for the j^{th} ADC and w_k the unknown k^{th} weight for each j^{th} normalized signal ($S_{j,k}^{\text{high}}/S_{j,k}^{\text{low}}$), corresponding to the k^{th} centroid.

To provide compact metrics, the resulting w^{pt} (Figure 1C, v) was employed to weight the sum of the median values (according to internal consistency tests, see paragraph 2.4) of the microstructural features (D, vf, R) from each cluster (Figure 1C, vi). Additionally, as previously proposed for prostate cancer^[39], the apparent cellularity was derived as $\rho_{app} = vf/R^3$ to provide a more interpretable clinical parameter.

Therefore, starting from three ADC values, a median value of D , v_f , R and ρ_{app} , respectively, was computed.

2.4 EXPERIMENTS

Internal consistency. The internal consistency of the workflow was evaluated by iteratively considering a centroid of the simulated partitioned data as input data (i.e. Figure 1B). In this case, the estimated weights were expected to be non-zero only for the partition corresponding to the centroid that was given as input. Also, the microstructural features computed for each centroid were compared with the available ground truth values in terms of root mean squared error (RMSE). At this stage, mean, median and mode were tested as candidate metrics to represent microstructural features distributions.

Imaging markers of tumour microstructure. The overall procedure was applied both to the median GTV signal and voxel-wise to produce quantitative maps of estimated microstructural markers (D , v_f , R and ρ_{app}), for each patient. Histogram-based metrics (median, interquartile range (iqr), skewness, kurtosis) were considered for both median and voxel-wise analyses. In both scenarios, meningothelial and atypical meningioma patients, the two groups with the highest prevalence, were compared for differences in ADC (200,400,1000) and microstructural markers using a Mann-Whitney U-test ($\alpha=0.05$). The sample size of the other histological groups (i.e. fibroblastic, psammomatous, transitional, anaplastic) was not large enough to perform meaningful statistical analyses on single groups. However, they were included when testing for statistical differences in terms of tumour grade WHO I vs. WHO II/III (Mann-Whitney U-test, $\alpha=0.05$). A receiver operating characteristic (ROC) analysis was carried out to gain insights into the capabilities of the measured median ADC and estimated microstructural markers in discriminating patients for tumour subtypes (meningothelial vs. atypical) or grade (WHO I vs. II/III). A logistic regression model provided the probabilities that patients belonged to a class, which were used to build ROC curves. Sensitivity (se) and specificity (sp) were selected according to Youden's J index^[40]. To avoid detecting spurious differences, ADC values from white matter regions, automatically contoured^[41], were also compared across histological sub-types and grades.

Longitudinal analysis. For patients for which the risk score was available ($n=25$, meningothelial and atypical) follow-up (fup) DW-MRI was analysed and compared with the baseline. Temporal percent differences in histogram metrics (m) were computed, as $100 \cdot (m_{fup} - m_{baseline}) / (m_{fup} + m_{baseline}) / 2$. The ability of ADC and microstructural parameters to distinguish between high- and low-risk patients was evaluated through statistical (Mann-Whitney U-test $\alpha=0.05$) and ROC analyses.

3 RESULTS

Internal consistency. The internal consistency analysis showed that the estimated microstructural parameters followed the ranges of true values (Figure S5). When comparing the microstructural features to the true ones, RMSE was $0.25 \mu\text{m}^2/\text{ms}$ for D, 0.05 for vf and $2.79 \mu\text{m}$ for R (Table S1). Given the non-parametric distributions and the RMSE, median values, instead of mean or mode, were chosen to encapsulate the non-parametric distributions of microstructural parameters.

Imaging markers of tumour microstructure. When analysing patient data, median ADC values ($p=0.007$, for ADC(200,400,1000)) were found to significantly differ between meningothelial and atypical meningioma patients (Figure 2a), together with D ($p=0.006$), vf ($p=0.006$), R ($p=0.032$) and ρ_{app} ($p=0.025$). The results reported are for ADC(200,400,1000), but similar results (Figure S7) were obtained for ADC(200,1000) and ADC(400,1000). Median (iqr) values are reported in supplementary materials (Table S2). The same trend was observed at the voxel-wise level (Figure 3), when comparing median values computed from ADC, D, vf, R and ρ_{app} maps ($p=0.003$ for vf, $p=0.002$ for others) of the lesions. As for other histogram-based metrics (Table S3), the two histological groups significantly differed in terms of skewness for ADC ($p=0.005$), D ($p=0.007$), vf ($p=0.011$), R ($p=0.007$) and ρ_{app} ($p=0.001$), and in terms of kurtosis for R ($p=0.045$) and ρ_{app} ($p=0.003$). Microstructural parameters were also estimated for tumours of other histological subtypes (Figure S6). Due to the small sample sizes, they could not be singularly analysed, but contributed to the comparison of WHO I vs. WHO II/III patients (Figure 2b), for which median values for ADC, D, vf, R and ρ_{app} were observed to significantly differ (Table S4). Moreover, no difference between sub-types or grades was found in the normally appearing white matter (Figure S9). The voxel-wise analysis (Figure 3) confirmed the results obtained for median values and showed significance (Table S5) also in terms of skewness for ADC ($p=0.005$), D ($p=0.005$), vf ($p=0.007$), R ($p=0.007$) and ρ_{app} ($p=0.002$) distributions, as well as in terms of kurtosis for R ($p=0.040$) and ρ_{app} ($p=0.022$). From ROC analyses (Figure 4), D and vf showed lower sensitivity (0.70) but higher specificity (0.93) with respect to ADC, R and ρ_{app} ($\text{sp}=0.80$, $\text{se}=0.80$) in dividing meningothelial from atypical meningiomas. When differentiating for tumour grade, the ROC analysis showed that D and vf had the highest sensitivity ($\text{se}=0.91$) and R and ρ_{app} the highest specificity ($\text{sp}=0.75$), against ADC ($\text{se}=0.87$, $\text{sp}=0.67$). More details are reported in the supplementary material (Table S6-S7).

Longitudinal analysis. Temporal percent differences median values for all parameters were significantly different between low- and high-risk patients, being ADC, D and R higher and vf and ρ_{app} lower at follow-up for high-risk patients (Figure 5). Changes in kurtosis and skewness for ρ_{app} maps differed significantly

($p=0.014$, $p=0.004$) between risk groups. Furthermore, the latter showed the highest AUC (0.90, Figure 6) and Youden's J index (0.75) with respect to histogram statistics from all parameters (Table S8).

4 DISCUSSION

A set of microstructural markers of potential interest for proton therapy (water intrinsic diffusivity D , cell volume fraction vf , radius R and apparent cellularity ρ_{app}) were estimated from routinely acquired ADC for a cohort of patients affected by meningioma, by matching measured with simulated ADC. This enabled the interpretation of ADC information from a microstructural perspective as a way to provide novel insights for the development of personalized proton treatments. It also represented an attempt to decode the microstructural information embedded in the ADC, which is not a specific marker since many combinations of different microstructural features can give the same ADC.

The estimates were tested in terms of internal consistency to assess the confidence in the inferred microstructural features and the median value of each distribution was employed to estimate the corresponding marker of tumour's microstructure. As such, the chosen microstructural markers (D , vf and R) turned out to stratify patients in different groups.

The main advantage of the proposed work is that it can provide discriminative imaging markers of tumour microstructure from a relatively unspecific metric, as the ADC is, that may help improving advanced radiotherapy treatments. Such markers should be interpreted as quantitative measurements of MR-apparent tissue features, following the widespread definition of quantitative imaging biomarkers^[42], for which these are objectively measured quantitative indices that may depend on the acquisition protocol. For example, vf may depend on the acquisition echo time, since it is a relaxation-weighted estimate of the real cellular volume fraction. As such, the clinical usefulness of the proposed work was shown for specific use cases, i.e. meningioma grading and treatment monitoring, but it may be straightforwardly applied to retrospectively analyse conventional ADC data in particle therapy applications.

Since patients eligible for proton therapy often present radioresistant and recurrent lesions^[8] for which biopsies are difficult to obtain, the distinct microstructural characteristics across tumour grades^[13] require to be non-invasively investigated as a support for the treatment decision-making process. In the patients' cohort here examined, only meningothelial and atypical meningioma subtypes allowed a meaningful statistical analysis. ADC could discriminate between the two groups, confirming its debated usefulness as a biomarker^[43,44], and such capability was enhanced by the quantitative microstructural features from the proposed method. Specifically, D and R were higher for meningothelial patients, whereas vf was higher

for atypical ones. These results agree with histopathological observations from the literature, which suggests that meningothelial lesions show bigger and less dense cells with respect to high grades ones^[33]. Similarly, the estimated ρ_{app} showed an inverse relationship with the ADC, as also observed in studies from the literature^[45], and confirmed higher cellularity to be present in more aggressive tumour types. Other histological groups were poorly represented in terms of sample size (Table 1) and only general comments can be made: anaplastic (WHO III) meningiomas exhibited an incoherent behaviour, whereas fibroblastic, transitional and psammomatous (WHO I subtypes) meningiomas showed intermediate D, vf and R, laying between meningothelial (WHO I) and atypical (WHO II). These results were also confirmed by the comparison of low- (WHO I) and high-grade (WHO II/III) lesions, considering that meningothelial and atypical meningiomas represented the largest components of low- and high-grade groups, respectively. The discriminative capabilities of ADC and inferred microstructural features were overall similar, but ROC analyses show (i) higher specificity of D and vf in discriminating histological subtypes and (ii) higher sensitivity of D and vf and higher specificity of R and ρ_{app} in discriminating tumour grades, compared to conventional ADC.

The voxel-wise analysis provided histogram-based parameters that may detect local characteristics of cancer tissue^[46], which could have been missed when analysing the median tumour behaviour. The asymmetry of ADC and microstructural parameters distributions represented by the skewness was indeed found to significantly differentiate patients' groups, being higher for ADC, D and R, and lower for vf in high-grade meningiomas with respect to low-grade ones. These preliminary results support the idea of detecting patterns of heterogeneity corresponding to different tumour sub-regions, which could be used to target specific areas with dose painting in proton active beam scanning systems^[47], for example in regions of increased cellularity^[48] as highlighted by ρ_{app} maps (Figure 3). However, the identification of biologically aggressive areas to be targeted is still an open research question and requires the implementation of appropriate longitudinal studies^[49].

Prospective longitudinal studies could help defining such areas from radiological imaging and, if combined to quantitative markers of tumour microstructure, as those here proposed, could provide insights into tumour microstructural changes due to proton therapy. From the preliminary longitudinal analysis, the conventional ADC and the microstructural parameters derived in this work showed greater changes in median values at three months after therapy in high-risk patients. Both risk groups presented increased diffusivity and decreased cellularity, which overall agree with apoptotic pathways typically induced by fractionated conventional radiotherapy. However, the damage and repair mechanisms triggered by protons are different in nature (i.e. DNA damage and immuno-cell recruitment) and may occur at

different timings with respect to X-ray radiotherapy^[50] which, in turn, could lead to further changes in structural properties that cannot be disentangled using unspecific conventional ADC measurements. The ADC is known to be a sensitive but not specific parameter, meaning that an increased ADC cannot distinguish, for example, between increased cell death or increased vasogenic oedema. Quantitative markers of tumour microstructure, as those here derived (i.e. v_f , R and ρ_{app}), can instead aid in disentangling structural alterations following radiotherapy at the voxel level. As a matter of fact, the parameter that better distinguished between risk groups was the skewness of ρ_{app} histograms, suggesting that the apparent cellularity ρ_{app} may be a useful marker of early microstructural regional changes of tumour response due to radiotherapy. It should be noted, however, that a limitation of the current longitudinal analysis is the unbalanced composition of our cohort: four out of five high-risk meningiomas were atypical and the fact that they may undergo death pathways different from meningothelial ones could have confounded the analysis of the response. Additionally, longer follow-up times are needed for a more robust assessment of risks following radiotherapy. Based on the promising results of this work, future studies will harness a larger and better stratified cohort as well as longer follow-up periods to address these limitations.

Future developments should also focus on the histological validation of the quantitative nature of the estimated parameters, even if a limited number of studies compared in-vivo DW-MRI parameters to histological features^[43,51,52] due to the difficulties in data acquisition^[53] and validation. Such validation would allow confirming or adapting the ranges of plausible microstructural markers of the synthetic cellular packings, which were defined in agreement with the available literature^[33,34]. However, performing such comparison could be even more challenging for brain tumours treated with proton therapy, for which histological data is not typically acquired, especially at follow-up times, but direct validation against histopathological imaging^[52] should be investigated before the proposed microstructural markers can be employed in any specific clinical application.

Technical aspects could be further developed and enhanced, too. Firstly, the synthetic cellular packings could be refined to fully exploit the potential realism that the proposed method unlocks, for example when accounting for exchange effects. Also, the exploration of other inference methods (e.g. machine learning^[54]) could be investigated. Furthermore, the DW-MRI sequence was generally tuned to neuro-oncology studies (e.g. maximum b-value=1000 s/mm², signal averaging along three orthogonal directions), but not to meningiomas biophysical characteristics^[25], which may benefit from differentiation among local structural anisotropies^[18]. A wider range of b-values could be considered. By using b-values greater than 1000 s/mm², the signal could show a non-gaussian behaviour (e.g. kurtosis) and the ADC would be ill-

defined. By using b-values below 200 s/mm², vasculature effects would have an impact on the estimation of the ADC and the synthetic cellular packings would need to include capillary networks. Future work will aim to address the realism of models of tumour structure and vascular networks, which could improve the description of meningiomas' microenvironment and its influence on tumour evolution. As such, the proposed approach could be extended to estimate structural heterogeneity (such as fractional anisotropy from DTI or kurtosis from DKI) or vascular descriptors (such as perfusion fraction from IVIM^[55], vascular fraction from an adapted version of the VERDICT model^[26]) and oedema regions, which could better resolve the inherent ambiguity of the ADC-microstructure relationship. However, this would require advanced MRI sequences, potentially longer to acquire, which are not currently widespread in clinical workflows for proton therapy, in which time is more favourably allocated to X-ray imaging. In this context, faster DW-MRI sequences and methods able to interpret ADC ambiguities by deriving specific microstructural parameters, like the one here proposed, may find wider applicability.

5 CONCLUSIONS

In this work, we derive microstructural markers from ADC to support personalized proton therapy for treatment planning and monitoring. This method successfully allowed to differentiate low- and high-grade meningiomas with higher specificity than ADC and it is put forward to quantitatively describe tumour microstructure. Even if further validation is needed, it potentially allows to retrospectively mine already acquired data in, but not limited to, radiation and proton therapy for which long outcome information may be available, and to better understand treatments effects at the microscale level.

Acknowledgements: M.P. was supported by EPSRC EP/N018702-1 and the UKRI Future Leaders Fellowship MR/T020296/1.

Conflict of interest Statement: The authors have no relevant conflicts of interest to disclose.

REFERENCES

1. Durante M, Orecchia R, Loeffler JS. Charged-particle therapy in cancer: clinical uses and future perspectives. Nat Rev Clin Oncol [Internet] 2017;14(8):483–95. Available from: <http://dx.doi.org/10.1038/nrclinonc.2017.30>
2. Jaffray DA. Image-guided radiotherapy: From current concept to future perspectives. Nat Rev Clin

- Oncol [Internet] 2012;9(12):688–99. Available from: <http://dx.doi.org/10.1038/nrclinonc.2012.194>
3. Kurz C, Buizza G, Landry G, Kamp F, Rabe M, Paganelli C, et al. Medical physics challenges in clinical MR-guided radiotherapy. Radiat Oncol [Internet] 2020;15(1):93. Available from: <https://ro-journal.biomedcentral.com/articles/10.1186/s13014-020-01524-4>
 4. Louis DN, Perry A, Reifenberger G, von Deimling A, Figarella-Branger D, Cavenee WK, et al. The 2016 World Health Organization Classification of Tumors of the Central Nervous System: a summary. Acta Neuropathol [Internet] 2016;131(6):803–20. Available from: <http://link.springer.com/10.1007/s00401-016-1545-1>
 5. Voß KM, Spille DC, Sauerland C, Suero Molina E, Brokinkel C, Paulus W, et al. The Simpson grading in meningioma surgery: does the tumor location influence the prognostic value? J Neurooncol [Internet] 2017;133(3):641–51. Available from: <http://link.springer.com/10.1007/s11060-017-2481-1>
 6. Weber DC, Ares C, Villa S, Peerdeman SM, Renard L, Baumert BG, et al. Adjuvant postoperative high-dose radiotherapy for atypical and malignant meningioma: A phase-II parallel non-randomized and observation study (EORTC 22042-26042). Radiother Oncol [Internet] 2018;128(2):260–5. Available from: <https://doi.org/10.1016/j.radonc.2018.06.018>
 7. Weber DC, Schneider R, Goitein G, Koch T, Ares C, Geismar JH, et al. Spot Scanning-Based Proton Therapy for Intracranial Meningioma: Long-Term Results From the Paul Scherrer Institute. Int J Radiat Oncol [Internet] 2012;83(3):865–71. Available from: <http://dx.doi.org/10.1016/j.ijrobp.2011.08.027>
 8. Coggins WS, Pham NK, Nguyen A V., Branch DW, Guillet JY, Korst G, et al. A Systematic Review of Ion Radiotherapy in Maintaining Local Control Regarding Atypical and Anaplastic Meningiomas. World Neurosurg [Internet] 2019;132:282–91. Available from: <https://doi.org/10.1016/j.wneu.2019.08.149>
 9. Rackwitz T, Debus J. Clinical applications of proton and carbon ion therapy. Semin Oncol [Internet] 2019;46(3):226–32. Available from: <https://doi.org/10.1053/j.seminoncol.2019.07.005>
 10. Barresi V, Caffo M, Tuccari G. Classification of human meningiomas: lights, shadows, and future perspectives. J Neurosci Res 2016;94(12):1604–12.
 11. Harter PN, Braun Y, Plate KH. Classification of meningiomas—advances and controversies. Chinese

- Clin Oncol [Internet] 2017;6(S1):S2–S2. Available from: <http://cco.amegroups.com/article/view/15104/15711>
12. Surov A, Ginat DT, Lim T, Cabada T, Baskan O, Schob S, et al. Histogram Analysis Parameters Apparent Diffusion Coefficient for Distinguishing High and Low-Grade Meningiomas: A Multicenter Study. Transl Oncol [Internet] 2018;11(5):1074–9. Available from: <https://doi.org/10.1016/j.tranon.2018.06.010>
13. Zhang T, Yu J, Wang Y, Yin D, Fang L. WHO grade I meningioma subtypes: MRI features and pathological analysis. Life Sci [Internet] 2018;213(August):50–6. Available from: <https://doi.org/10.1016/j.lfs.2018.08.061>
14. Rogers L, Gilbert M, Vogelbaum MA. Intracranial meningiomas of atypical (WHO grade II) histology. J Neurooncol [Internet] 2010;99(3):393–405. Available from: <http://link.springer.com/10.1007/s11060-010-0343-1>
15. Zampini MA, Buizza G, Paganelli C, Fontana G, D'Ippolito E, Valvo F, et al. Perfusion and diffusion in meningioma tumors: a preliminary multiparametric analysis with Dynamic Susceptibility Contrast and IntraVoxel Incoherent Motion MRI. Magn Reson Imaging [Internet] 2020;67(November 2019):69–78. Available from: <https://linkinghub.elsevier.com/retrieve/pii/S0730725X19303509>
16. Moffat BA, Chenevert TL, Lawrence TS, Meyer CR, Johnson TD, Dong Q, et al. Functional diffusion map: A noninvasive MRI biomarker for early stratification of clinical brain tumor response. Proc Natl Acad Sci [Internet] 2005;102(15):5524–9. Available from: <http://www.pnas.org/cgi/doi/10.1073/pnas.0501532102>
17. Lin L, Bhawana R, Xue Y, Duan Q, Jiang R, Chen H, et al. Comparative Analysis of Diffusional Kurtosis Imaging, Diffusion Tensor Imaging, and Diffusion-Weighted Imaging in Grading and Assessing Cellular Proliferation of Meningiomas. Am J Neuroradiol [Internet] 2018;39(6):1032–8. Available from: <http://www.ajnr.org/lookup/doi/10.3174/ajnr.A5662>
18. Szczepankiewicz F, van Westen D, Englund E, Westin C-F, Ståhlberg F, Lätt J, et al. The link between diffusion MRI and tumor heterogeneity: Mapping cell eccentricity and density by diffusional variance decomposition (DIVIDE). Neuroimage [Internet] 2016;142:522–32. Available from: <https://linkinghub.elsevier.com/retrieve/pii/S1053811916303457>
19. Aslan K, Gunbey HP, Tomak L, Incesu L. The diagnostic value of using combined MR diffusion tensor imaging parameters to differentiate between low- and high-grade meningioma. Br J Radiol

2018;(January):20180088.

20. Gühr GA, Horvath-Rizea D, Garnov N, Kohlhof-Meinecke P, Ganslandt O, Henkes H, et al. Diffusion Profiling via a Histogram Approach Distinguishes Low-grade from High-grade Meningiomas, Can Reflect the Respective Proliferative Potential and Progesterone Receptor Status. *Mol Imaging Biol* [Internet] 2018;20(4):632–40. Available from: <http://link.springer.com/10.1007/s11307-018-1166-2>
21. Nilsson M, Englund E, Szczepankiewicz F, van Westen D, Sundgren PC. Imaging brain tumour microstructure. *Neuroimage* [Internet] 2018;182(May):232–50. Available from: <https://doi.org/10.1016/j.neuroimage.2018.04.075>
22. Wu W, Miller KL. Image formation in diffusion MRI: A review of recent technical developments. *J Magn Reson Imaging* 2017;46(3):646–62.
23. Padhani AR, Liu G, Mu-Koh D, Chenevert TL, Thoeny HC, Takahara T, et al. Diffusion-Weighted Magnetic Resonance Imaging as a Cancer Biomarker: Consensus and Recommendations. *Neoplasia* [Internet] 2009;11(2):102–25. Available from: <https://linkinghub.elsevier.com/retrieve/pii/S1476558609800249>
24. Novikov DS, Kiselev VG, Jespersen SN. On modeling. *Magn Reson Med* 2018;79(6):3172–93.
25. Tang L, Zhou XJ. Diffusion MRI of cancer: From low to high b-values. *J Magn Reson Imaging* 2019;49(1):23–40.
26. Panagiotaki E, Walker-Samuel S, Siow B, Johnson SP, Rajkumar V, Pedley RB, et al. Noninvasive Quantification of Solid Tumor Microstructure Using VERDICT MRI. *Cancer Res* [Internet] 2014;74(7):1902–12. Available from: <http://cancerres.aacrjournals.org/cgi/doi/10.1158/0008-5472.CAN-13-2511>
27. Le Bihan D. What can we see with IVIM MRI? *Neuroimage* [Internet] 2017;(December 2017):1–12. Available from: <https://doi.org/10.1016/j.neuroimage.2017.12.062>
28. Reynaud O. Time-Dependent Diffusion MRI in Cancer: Tissue Modeling and Applications. *Front Phys* 2017;5(November):1–16.
29. Tommasino F, Nahum A, Cella L. Increasing the power of tumour control and normal tissue complication probability modelling in radiotherapy: recent trends and current issues. *Transl Cancer Res* [Internet] 2017;6(S5):S807–21. Available from:

<http://tcr.amegroups.com/article/view/14116/11797>

30. Buizza G, Molinelli S, D'Ippolito E, Fontana G, Pella A, Valvo F, et al. MRI-based tumour control probability in skull-base chordomas treated with carbon-ion therapy. *Radiother Oncol* [Internet] 2019;137:32–7. Available from: <https://doi.org/10.1016/j.radonc.2019.04.018>
31. van der Heide UA, Houweling AC, Groenendaal G, Beets-Tan RGH, Lambin P. Functional MRI for radiotherapy dose painting. *Magn Reson Imaging* [Internet] 2012;30(9):1216–23. Available from: <http://dx.doi.org/10.1016/j.mri.2012.04.010>
32. Shackleford J, Shusharina N, Verberg J. Plastimatch 1.6: current capabilities and future directions. *Proc MICCAI 2012*; (July 2017).
33. Pećina-Šlaus N, Kafka A, Lechpammer M. Molecular Genetics of Intracranial Meningiomas with Emphasis on Canonical Wnt Signalling. *Cancers (Basel)* [Internet] 2016;8(7):67. Available from: <https://www.ncbi.nlm.nih.gov/pubmed/27429002>
34. Roberts TA, Hyare H, Agliardi G, Hipwell B, D'Esposito A, Ianus A, et al. Noninvasive diffusion magnetic resonance imaging of brain tumour cell size for the early detection of therapeutic response. *Sci Rep* [Internet] 2020;10(1):9223. Available from: <http://www.nature.com/articles/s41598-020-65956-4>
35. Donev A, Torquato S, Stillinger F. Neighbor list collision-driven molecular dynamics simulation for nonspherical hard particles.II. Applications to ellipses and ellipsoids. *J Comput Phys* [Internet] 2005;202(2):765–93. Available from: <https://linkinghub.elsevier.com/retrieve/pii/S0021999104003948>
36. Blender Online Community. Blender - a 3D modelling and rendering package [Internet]. 2017; Available from: <http://www.blender.org>
37. Hall MG, Alexander DC. Convergence and Parameter Choice for Monte-Carlo Simulations of Diffusion MRI. *IEEE Trans Med Imaging* 2009;28(9):1354–64.
38. Cook P a, Bai Y, Seunarine KK, Hall MG, Parker GJ, Alexander DC. Camino: Open-Source Diffusion-MRI Reconstruction and Processing. *14th Sci Meet Int Soc Magn Reson Med* 2006;14:2759.
39. Panagiotaki E, Chan RW, Dikaio N, Ahmed HU, O'Callaghan J, Freeman A, et al. Microstructural Characterization of Normal and Malignant Human Prostate Tissue With Vascular, Extracellular, and Restricted Diffusion for Cytometry in Tumours Magnetic Resonance Imaging. *Invest Radiol*

- [Internet] 2015;50(4):218–27. Available from: <http://journals.lww.com/00004424-201504000-00006>
40. Youden WJ. Index for rating diagnostic tests. *Cancer* [Internet] 1950;3(1):32–5. Available from: [https://doi.org/10.1002/1097-0142\(1950\)3:1%3C32::AID-CNCR2820030106%3E3.0.CO](https://doi.org/10.1002/1097-0142(1950)3:1%3C32::AID-CNCR2820030106%3E3.0.CO)
41. Li C, Gore JC, Davatzikos C. Multiplicative intrinsic component optimization (MICO) for MRI bias field estimation and tissue segmentation. *Magn Reson Imaging* [Internet] 2014;32(7):913–23. Available from: <http://dx.doi.org/10.1016/j.mri.2014.03.010>
42. Kessler LG, Barnhart HX, Buckler AJ, Choudhury KR, Kondratovich M V., Toledano A, et al. The emerging science of quantitative imaging biomarkers terminology and definitions for scientific studies and regulatory submissions. *Stat Methods Med Res* 2015;24(1):9–26.
43. Yin B, Liu L, Zhang BY, Li YX, Li Y, Geng DY. Correlating apparent diffusion coefficients with histopathologic findings on meningiomas. *Eur J Radiol* [Internet] 2012;81(12):4050–6. Available from: <http://dx.doi.org/10.1016/j.ejrad.2012.06.002>
44. Nagar VA, Ye JR, Ng WH, Chan YH, Hui F, Lee CK, et al. Diffusion-Weighted MR Imaging: Diagnosing Atypical or Malignant Meningiomas and Detecting Tumor Dedifferentiation. *Am J Neuroradiol* [Internet] 2008;29(6):1147–52. Available from: <http://www.ajnr.org/lookup/doi/10.3174/ajnr.A0996>
45. Surov A, Meyer HJ, Wienke A. Correlation between apparent diffusion coefficient (ADC) and cellularity is different in several tumors: a meta-analysis. *Oncotarget* [Internet] 2017;8(35):59492–9. Available from: <http://www.oncotarget.com/fulltext/17752>
46. McHugh DJ, Lipowska-Bhalla G, Babur M, Watson Y, Peset I, Mistry HB, et al. Diffusion model comparison identifies distinct tumor sub-regions and tracks treatment response. *Magn Reson Med* [Internet] 2020;84(3):1250–63. Available from: <https://onlinelibrary.wiley.com/doi/abs/10.1002/mrm.28196>
47. Madani I, Lomax AJ, Albertini F, Trnková P, Weber DC. Dose-painting intensity-modulated proton therapy for intermediate- and high-risk meningioma. *Radiat Oncol* [Internet] 2015;10(1):1–7. Available from: ???
48. Orlandi M, Botti A, Sghedoni R, Cagni E, Ciammella P, Iotti C, et al. Feasibility of voxel-based Dose Painting for recurrent Glioblastoma guided by ADC values of Diffusion-Weighted MR imaging. *Phys*

- Medica [Internet] 2016;32(12):1651–8. Available from: <http://linkinghub.elsevier.com/retrieve/pii/S1120179716310845>
49. Orman AG, Pollack A, Stoyanova R, Wang K, Abramowitz M. A Phase 3 Randomized Trial of MRI-Mapped Dose-Escalated Salvage Radiation Therapy Postprostatectomy: The MAPS Trial, An Initial Dosimetric Assessment. *Int J Radiat Oncol* [Internet] 2014;90(1):S413–4. Available from: <https://linkinghub.elsevier.com/retrieve/pii/S0360301614019658>
 50. Ray S, Cekanaviciute E, Lima IP, Sørensen BS, Costes S V. Comparing Photon and Charged Particle Therapy Using DNA Damage Biomarkers. *Int J Part Ther* [Internet] 2018;5(1):15–24. Available from: <http://theijpt.org/doi/10.14338/IJPT-18-00018.1>
 51. Surov A, Caysa H, Wienke A, Spielmann RP, Fiedler E. Correlation Between Different ADC Fractions, Cell Count, Ki-67, Total Nucleic Areas and Average Nucleic Areas in Meningothelial Meningiomas. *Anticancer Res* [Internet] 2015;35(12):6841–6. Available from: <http://www.ncbi.nlm.nih.gov/pubmed/26637905>
 52. Gonzalez-Segura A, Morales JM, Gonzalez-Darder JM, Cardona-Marsal R, Lopez-Gines C, Cerda-Nicolas M, et al. Magnetic Resonance Microscopy at 14 Tesla and Correlative Histopathology of Human Brain Tumor Tissue. *PLoS One* [Internet] 2011;6(11):e27442. Available from: <https://dx.plos.org/10.1371/journal.pone.0027442>
 53. Commins DL, Atkinson RD, Burnett ME. Review of meningioma histopathology. *Neurosurg Focus* 2007;23(4):E3.
 54. Nedjati-Gilani GL, Schneider T, Hall MG, Cawley N, Hill I, Ciccarelli O, et al. Machine learning based compartment models with permeability for white matter microstructure imaging. *Neuroimage* [Internet] 2017;150(July 2016):119–35. Available from: <http://dx.doi.org/10.1016/j.neuroimage.2017.02.013>
 55. Togao O, Hiwatashi A, Yamashita K, Kikuchi K, Momosaka D, Yoshimoto K, et al. Measurement of the perfusion fraction in brain tumors with intravoxel incoherent motion MR imaging: validation with histopathologic vascular density in meningiomas. *Br J Radiol* [Internet] 2018;(January):20170912. Available from: <https://doi.org/10.1259/bjr.20170912>
 2. Jaffray DA. Image-guided radiotherapy: From current concept to future perspectives. *Nat Rev Clin*

- Oncol.* 2012;9(12):688-699. doi:10.1038/nrclinonc.2012.194
3. Kurz C, Buizza G, Landry G, et al. Medical physics challenges in clinical MR-guided radiotherapy. *Radiat Oncol.* 2020;15(1):93. doi:10.1186/s13014-020-01524-4
 4. Louis DN, Perry A, Reifenberger G, et al. The 2016 World Health Organization Classification of Tumors of the Central Nervous System: a summary. *Acta Neuropathol.* 2016;131(6):803-820. doi:10.1007/s00401-016-1545-1
 5. Voß KM, Spille DC, Sauerland C, et al. The Simpson grading in meningioma surgery: does the tumor location influence the prognostic value? *J Neurooncol.* 2017;133(3):641-651. doi:10.1007/s11060-017-2481-1
 6. Weber DC, Ares C, Villa S, et al. Adjuvant postoperative high-dose radiotherapy for atypical and malignant meningioma: A phase-II parallel non-randomized and observation study (EORTC 22042-26042). *Radiother Oncol.* 2018;128(2):260-265. doi:10.1016/j.radonc.2018.06.018
 7. Weber DC, Schneider R, Goitein G, et al. Spot Scanning-Based Proton Therapy for Intracranial Meningioma: Long-Term Results From the Paul Scherrer Institute. *Int J Radiat Oncol.* 2012;83(3):865-871. doi:10.1016/j.ijrobp.2011.08.027
 8. Coggins WS, Pham NK, Nguyen A V., et al. A Systematic Review of Ion Radiotherapy in Maintaining Local Control Regarding Atypical and Anaplastic Meningiomas. *World Neurosurg.* 2019;132:282-291. doi:10.1016/j.wneu.2019.08.149
 9. Rackwitz T, Debus J. Clinical applications of proton and carbon ion therapy. *Semin Oncol.* 2019;46(3):226-232. doi:10.1053/j.seminoncol.2019.07.005
 10. Barresi V, Caffo M, Tuccari G. Classification of human meningiomas: lights, shadows, and future perspectives. *J Neurosci Res.* 2016;94(12):1604-1612. doi:10.1002/jnr.23801
 11. Harter PN, Braun Y, Plate KH. Classification of meningiomas—advances and controversies. *Chinese Clin Oncol.* 2017;6(S1):S2-S2. doi:10.21037/cco.2017.05.02
 12. Surov A, Ginat DT, Lim T, et al. Histogram Analysis Parameters Apparent Diffusion Coefficient for Distinguishing High and Low-Grade Meningiomas: A Multicenter Study. *Transl Oncol.* 2018;11(5):1074-1079. doi:10.1016/j.tranon.2018.06.010
 13. Zhang T, Yu J, Wang Y, Yin D, Fang L. WHO grade I meningioma subtypes: MRI features and

- pathological analysis. *Life Sci.* 2018;213(August):50-56. doi:10.1016/j.lfs.2018.08.061
14. Rogers L, Gilbert M, Vogelbaum MA. Intracranial meningiomas of atypical (WHO grade II) histology. *J Neurooncol.* 2010;99(3):393-405. doi:10.1007/s11060-010-0343-1
15. Zampini MA, Buizza G, Paganelli C, et al. Perfusion and diffusion in meningioma tumors: a preliminary multiparametric analysis with Dynamic Susceptibility Contrast and IntraVoxel Incoherent Motion MRI. *Magn Reson Imaging.* 2020;67(November 2019):69-78. doi:10.1016/j.mri.2019.12.003
16. Moffat BA, Chenevert TL, Lawrence TS, et al. Functional diffusion map: A noninvasive MRI biomarker for early stratification of clinical brain tumor response. *Proc Natl Acad Sci.* 2005;102(15):5524-5529. doi:10.1073/pnas.0501532102
17. Lin L, Bhawana R, Xue Y, et al. Comparative Analysis of Diffusional Kurtosis Imaging, Diffusion Tensor Imaging, and Diffusion-Weighted Imaging in Grading and Assessing Cellular Proliferation of Meningiomas. *Am J Neuroradiol.* 2018;39(6):1032-1038. doi:10.3174/ajnr.A5662
18. Szczepankiewicz F, van Westen D, Englund E, et al. The link between diffusion MRI and tumor heterogeneity: Mapping cell eccentricity and density by diffusional variance decomposition (DIVIDE). *Neuroimage.* 2016;142:522-532. doi:10.1016/j.neuroimage.2016.07.038
19. Aslan K, Gunbey HP, Tomak L, Incesu L. The diagnostic value of using combined MR diffusion tensor imaging parameters to differentiate between low- and high-grade meningioma. *Br J Radiol.* 2018;(January):20180088. doi:10.1259/bjr.20180088
20. Gühr GA, Horvath-Rizea D, Garnov N, et al. Diffusion Profiling via a Histogram Approach Distinguishes Low-grade from High-grade Meningiomas, Can Reflect the Respective Proliferative Potential and Progesterone Receptor Status. *Mol Imaging Biol.* 2018;20(4):632-640. doi:10.1007/s11307-018-1166-2
21. Nilsson M, Englund E, Szczepankiewicz F, van Westen D, Sundgren PC. Imaging brain tumour microstructure. *Neuroimage.* 2018;182(May):232-250. doi:10.1016/j.neuroimage.2018.04.075
22. Wu W, Miller KL. Image formation in diffusion MRI: A review of recent technical developments. *J Magn Reson Imaging.* 2017;46(3):646-662. doi:10.1002/jmri.25664
23. Padhani AR, Liu G, Mu-Koh D, et al. Diffusion-Weighted Magnetic Resonance Imaging as a Cancer Biomarker: Consensus and Recommendations. *Neoplasia.* 2009;11(2):102-125.

doi:10.1593/neo.81328

24. Novikov DS, Kiselev VG, Jespersen SN. On modeling. *Magn Reson Med*. 2018;79(6):3172-3193. doi:10.1002/mrm.27101
25. Tang L, Zhou XJ. Diffusion MRI of cancer: From low to high b-values. *J Magn Reson Imaging*. 2019;49(1):23-40. doi:10.1002/jmri.26293
26. Panagiotaki E, Walker-Samuel S, Siow B, et al. Noninvasive Quantification of Solid Tumor Microstructure Using VERDICT MRI. *Cancer Res*. 2014;74(7):1902-1912. doi:10.1158/0008-5472.CAN-13-2511
27. Le Bihan D. What can we see with IVIM MRI? *Neuroimage*. 2017;(December 2017):1-12. doi:10.1016/j.neuroimage.2017.12.062
28. Reynaud O. Time-Dependent Diffusion MRI in Cancer: Tissue Modeling and Applications. *Front Phys*. 2017;5(November):1-16. doi:10.3389/fphy.2017.00058
29. Tommasino F, Nahum A, Cella L. Increasing the power of tumour control and normal tissue complication probability modelling in radiotherapy: recent trends and current issues. *Transl Cancer Res*. 2017;6(S5):S807-S821. doi:10.21037/tcr.2017.06.03
30. Buizza G, Molinelli S, D'Ippolito E, et al. MRI-based tumour control probability in skull-base chordomas treated with carbon-ion therapy. *Radiother Oncol*. 2019;137:32-37. doi:10.1016/j.radonc.2019.04.018
31. van der Heide UA, Houweling AC, Groenendaal G, Beets-Tan RGH, Lambin P. Functional MRI for radiotherapy dose painting. *Magn Reson Imaging*. 2012;30(9):1216-1223. doi:10.1016/j.mri.2012.04.010
32. Shackleford J, Shusharina N, Verberg J. Plastimatch 1.6: current capabilities and future directions. *Proc MICCAI*. 2012;(July 2017).
33. Donev A, Torquato S, Stillinger F. Neighbor list collision-driven molecular dynamics simulation for nonspherical hard particles.II. Applications to ellipses and ellipsoids. *J Comput Phys*. 2005;202(2):765-793. doi:10.1016/S0021-9991(04)00394-8
34. Blender Online Community. Blender - a 3D modelling and rendering package. 2017. <http://www.blender.org>.

35. Hall MG, Alexander DC. Convergence and Parameter Choice for Monte-Carlo Simulations of Diffusion MRI. *IEEE Trans Med Imaging*. 2009;28(9):1354-1364. doi:10.1109/TMI.2009.2015756
36. Cook P a, Bai Y, Seunarine KK, Hall MG, Parker GJ, Alexander DC. Camino: Open-Source Diffusion-MRI Reconstruction and Processing. *14th Sci Meet Int Soc Magn Reson Med*. 2006;14:2759.
37. Panagiotaki E, Chan RW, Dikaio N, et al. Microstructural Characterization of Normal and Malignant Human Prostate Tissue With Vascular, Extracellular, and Restricted Diffusion for Cytometry in Tumours Magnetic Resonance Imaging. *Invest Radiol*. 2015;50(4):218-227. doi:10.1097/RLI.0000000000000115
38. Youden WJ. Index for rating diagnostic tests. *Cancer*. 1950;3(1):32-35. doi:10.1002/1097-0142(1950)3:1<32::AID-CNCR2820030106>3.0.CO;2-3
39. Yin B, Liu L, Zhang BY, Li YX, Li Y, Geng DY. Correlating apparent diffusion coefficients with histopathologic findings on meningiomas. *Eur J Radiol*. 2012;81(12):4050-4056. doi:10.1016/j.ejrad.2012.06.002
40. Nagar VA, Ye JR, Ng WH, et al. Diffusion-Weighted MR Imaging: Diagnosing Atypical or Malignant Meningiomas and Detecting Tumor Dedifferentiation. *Am J Neuroradiol*. 2008;29(6):1147-1152. doi:10.3174/ajnr.A0996
41. Pećina-Šlaus N, Kafka A, Lechpammer M. Molecular Genetics of Intracranial Meningiomas with Emphasis on Canonical Wnt Signalling. *Cancers (Basel)*. 2016;8(7):67. doi:10.3390/cancers8070067
42. Surov A, Meyer HJ, Wienke A. Correlation between apparent diffusion coefficient (ADC) and cellularity is different in several tumors: a meta-analysis. *Oncotarget*. 2017;8(35):59492-59499. doi:10.18632/oncotarget.17752
43. McHugh DJ, Lipowska-Bhalla G, Babur M, et al. Diffusion model comparison identifies distinct tumor sub-regions and tracks treatment response. *Magn Reson Med*. 2020;84(3):1250-1263. doi:10.1002/mrm.28196
44. Madani I, Lomax AJ, Albertini F, Trnková P, Weber DC. Dose-painting intensity-modulated proton therapy for intermediate- and high-risk meningioma. *Radiat Oncol*. 2015;10(1):1-7. doi:10.1186/s13014-015-0384-x
45. Orlandi M, Botti A, Sghedoni R, et al. Feasibility of voxel-based Dose Painting for recurrent Glioblastoma guided by ADC values of Diffusion-Weighted MR imaging. *Phys Medica*.

2016;32(12):1651-1658. doi:10.1016/j.ejmp.2016.11.106

46. Orman AG, Pollack A, Stoyanova R, Wang K, Abramowitz M. A Phase 3 Randomized Trial of MRI-Mapped Dose-Escalated Salvage Radiation Therapy Postprostatectomy: The MAPS Trial, An Initial Dosimetric Assessment. *Int J Radiat Oncol.* 2014;90(1):S413-S414. doi:10.1016/j.ijrobp.2014.05.1314
47. Ray S, Cekanaviciute E, Lima IP, Sørensen BS, Costes S V. Comparing Photon and Charged Particle Therapy Using DNA Damage Biomarkers. *Int J Part Ther.* 2018;5(1):15-24. doi:10.14338/IJPT-18-00018.1
48. Surov A, Caysa H, Wienke A, Spielmann RP, Fiedler E. Correlation Between Different ADC Fractions, Cell Count, Ki-67, Total Nucleic Areas and Average Nucleic Areas in Meningothelial Meningiomas. *Anticancer Res.* 2015;35(12):6841-6846. <http://www.ncbi.nlm.nih.gov/pubmed/26637905>.
49. Gonzalez-Segura A, Morales JM, Gonzalez-Darder JM, et al. Magnetic Resonance Microscopy at 14 Tesla and Correlative Histopathology of Human Brain Tumor Tissue. Bankiewicz K, ed. *PLoS One.* 2011;6(11):e27442. doi:10.1371/journal.pone.0027442
50. Commins DL, Atkinson RD, Burnett ME. Review of meningioma histopathology. *Neurosurg Focus.* 2007;23(4):E3. doi:10.3171/foc-07/10/e3
51. Nedjati-Gilani GL, Schneider T, Hall MG, et al. Machine learning based compartment models with permeability for white matter microstructure imaging. *Neuroimage.* 2017;150(July 2016):119-135. doi:10.1016/j.neuroimage.2017.02.013
52. Togao O, Hiwatashi A, Yamashita K, et al. Measurement of the perfusion fraction in brain tumors with intravoxel incoherent motion MR imaging: validation with histopathologic vascular density in meningiomas. *Br J Radiol.* 2018;(January):20170912. doi:10.1259/bjr.20170912

Figure Legends

Figure 1 - Schematic representation of the pipeline. Various steps are highlighted in different colours, as detailed by the top-right legend. Panel A shows how synthetic cellular packings and Monte Carlo (MC) simulations were used to generate simulation data (see paragraph 2.2). Panel B shows the input patient data (see paragraph 2.1). Panel C (see paragraph 2.3) describes how simulation and patient data were coupled: after clustering (i-iii) the simulation data in a 3D space (i.e., considering the three ADC values obtained using three combinations of b values: (200, 1000); (400,

1000) and (200, 400, 1000)), the optimizer (iv) exploited the centroid's ADC to estimate the best weights (v) that were used to compute (vi) microstructural features, for each patient.

Figure 2 - Boxplots for median values from ADC, diffusion coefficient (D), volume fraction (vf), radius (R) and apparent cellularity (ρ_{app}) with respect to histological sub-typing (a) and grading (b) tasks.

Figure 3 - Examples of voxel-wise maps of meningothelial (top row) and atypical (bottom row) meningioma, which differed for patterns in both the measured ADC and in the estimated diffusion coefficient (D), volume fraction (vf), cells' radius (R) and apparent cellularity (ρ_{app}). The estimated microstructural markers are displayed in the gross tumour volume (GTV) region, according to the colour scale displayed at the bottom and overlapped to a grayscale DW-MRI slice.

Figure 4 - ROC curves for median values from ADC, diffusion coefficient (D), volume fraction (vf), radius (R) and apparent cellularity (ρ) with respect to histological sub-typing (a) and grading (b) tasks.

Figure 5 - Temporal percent differences in ADC(200,400,1000), diffusion coefficient (D), volume fraction (vf), radius (R) and apparent cellularity (ρ_{app}) for low- and high-risk patients. Similar results were obtained for the other ADC values, calculated using the b-values combinations (200, 1000) and (400, 1000), see Figure S8.

Figure 6 - ROC curves for (a) median values from temporal percent differences in ADC, diffusion coefficient (D), volume fraction (vf), radius (R) and apparent cellularity (ρ), and (b) kurtosis, skewness and median values from temporal percent differences in apparent cellularity, with respect to the patient risk assessment task.

Table 1 – Clinical characteristics of the patient cohort. For categorical variables (gender, tumour grade, tumour subtype, tumour location, response risk score) frequencies and percentages (%) are reported. For continuous variables (age, tumour volume from MRI contouring, planning GTV, prescribed dose and fractionation scheme) mean and standard deviation (sd) are reported.

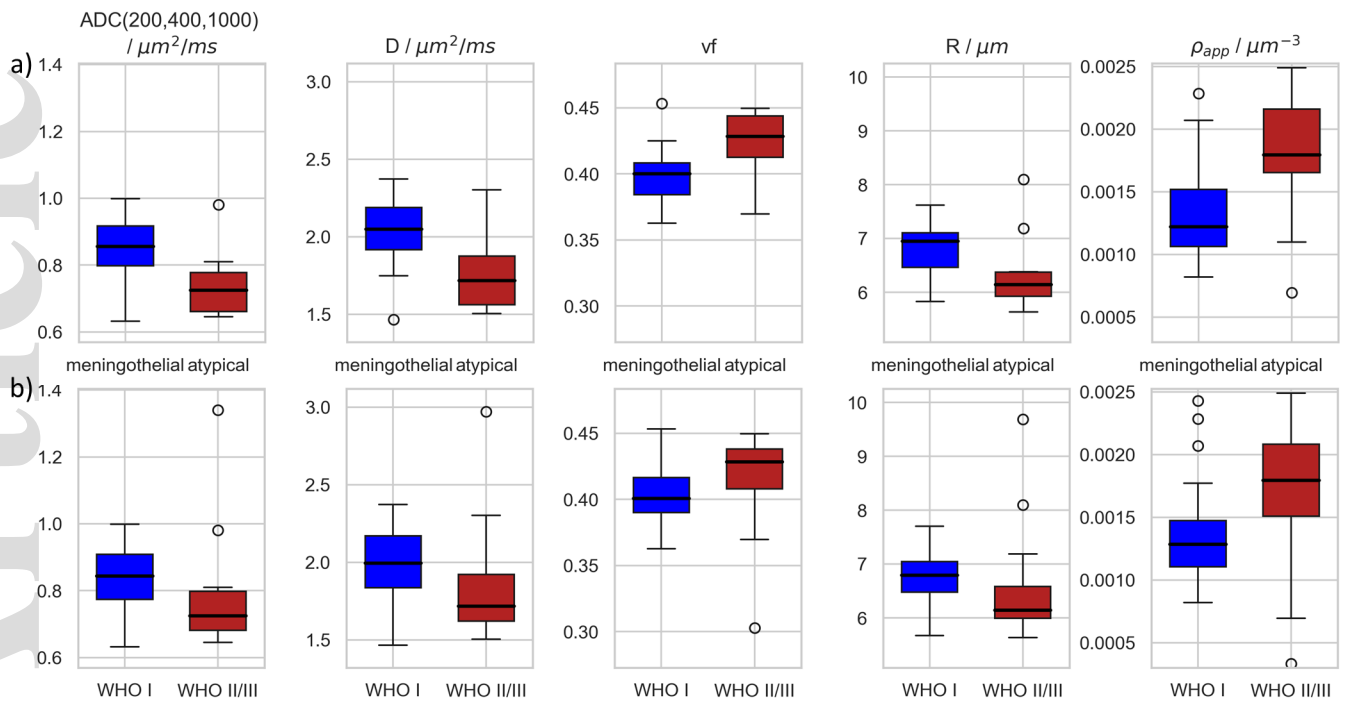
		frequency	%
Gender			
	female	18	51
	male	17	49
Grade	Subtype		
WHO I	meningothelial	15	43
	transitional	5	14
	fibroblastic	2	6
	psammomatous	1	3
WHO II	atypical	10	29
WHO III	anaplastic	2	6
Anatomical location			
	Skull-base	22	63
	Convexity	5	14
	Falx	6	17
	Posterior fossae	2	6
Response risk score			
	Low	20	80
	High	5	20
		mean	sd
	Age	57.7	14.7
	MRI-based GTV^a / cm³	20.2	31.6
	Planning GTV / cm³	62.2	77.4
	Prescribed dose / Gy(RBE)^b	52.5	8.5
	Fractionation / days	25.1	9.0

^aGTV=gross tumour volume; ^bGy(RBE)=RBE-weighted dose

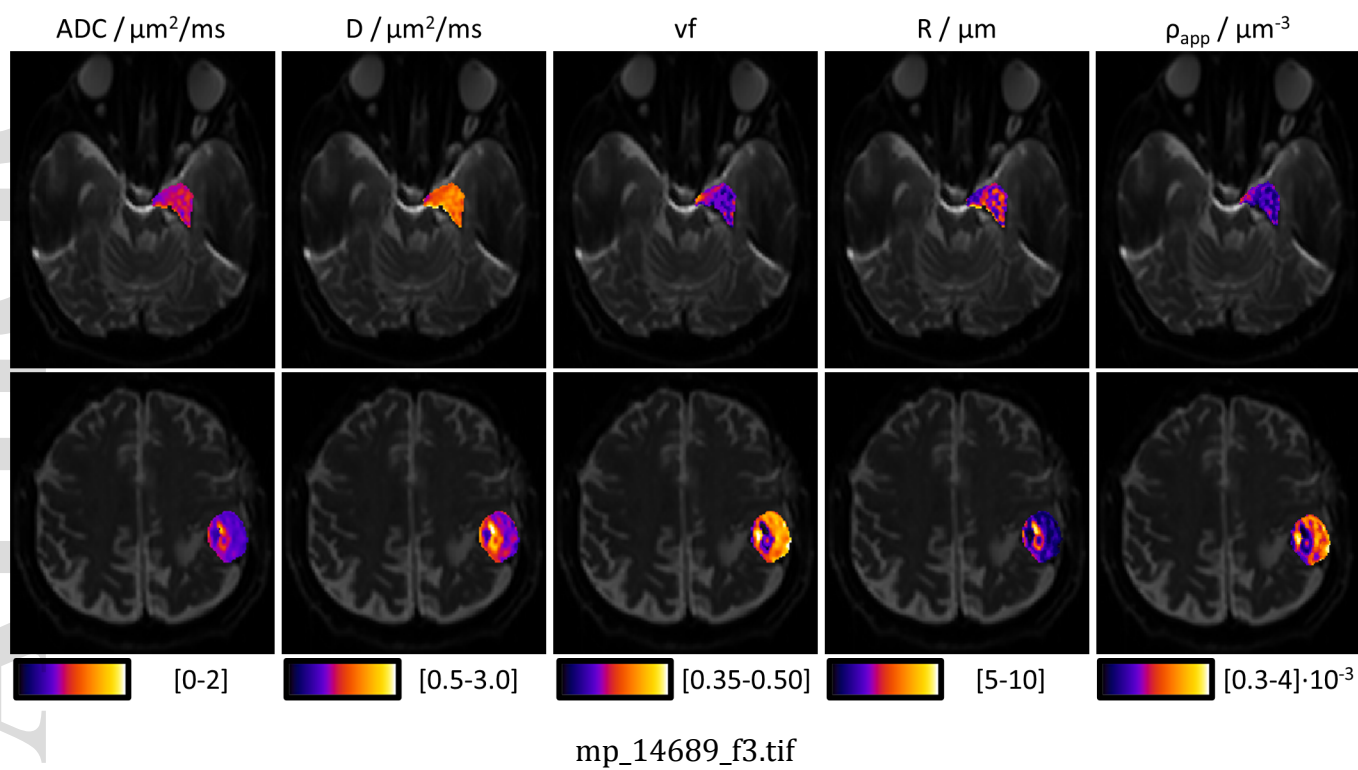
Table 2 – Geometrical properties (volume fraction (vf), radius (R)) and diffusion (D) and permeability (p) coefficients assigned to the synthetic cellular packings used for simulating DW-MRI signals. Mean, standard deviation (sd), range and mode of each parameter's distribution are reported. Additionally, the discrete values set for D, vf, R (shown as [start : step : stop]) and p (complete list {;}) are reported.

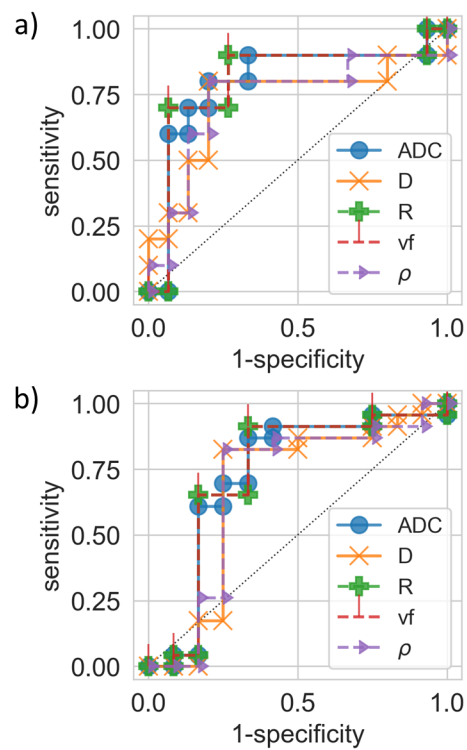
	vf	R / μm	D / $\mu\text{m}^2/\text{ms}$	p / 10^{-2} mm/s
mean	0.4	6.4	1.7	3.6
sd	0.1	2.7	0.9	3.3
range	0.3	7.6	2.5	9.2
mode	0.3	10	1.0	0
discrete values	[0.3 : 0.1 : 0.6]	[2.5 : 2.5 : 10]	[0.5 : 0.5 : 3.0]	{0; 1.3; 2.3; 5.7; 9.2}

^avf=volume fraction; ^bR=radius; ^cD=true diffusion coefficient; ^dp=permeability coefficient.

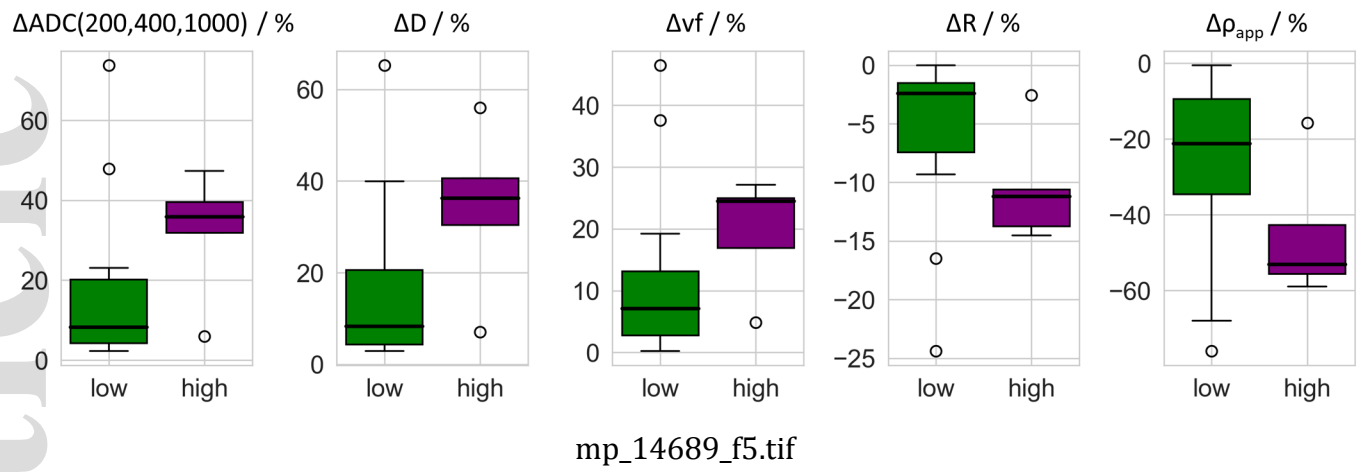


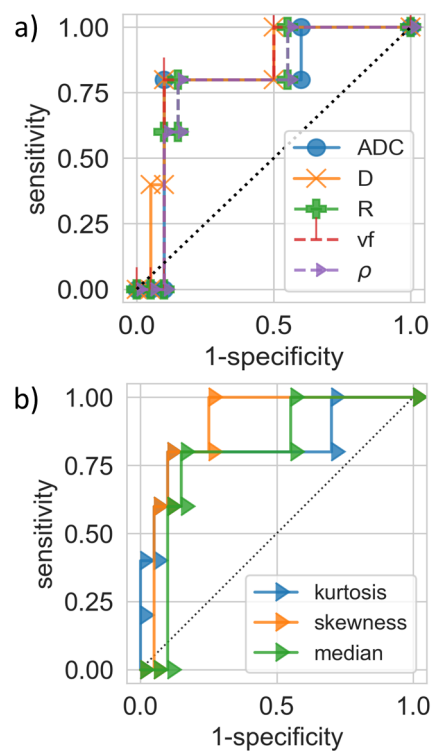
mp_14689_f2.tif





mp_14689_f4.tif





mp_14689_f6.tif